Kepler and STExTS Observations and Analysis of the Algol Variable KIC 201325107

John Paul Jones

Advisors: Dr. Richard Olenick and Mr. Arthur Sweeney

Submitted in partial fulfillment of the Bachelor of Science Degree in Physics at the

University of Dallas

January 2018

Abstract

We report the use of remote telescopes at the Dark Skies Observatory Collaborative near Ft. Davis, TX used to collect data in transiting exoplanet searches by the Small Telescope Exoplanet Transit Search (STExTS). We describe the use of AstroImageJ software to process data and analyze the known exoplanet HD189733b. We also present results from long cadence Kepler observations covering 64 days of the newly discovered Algol-type variable KIC 201325107. Using Peranso and O-C calculation for time series analysis, we detect an orbital period of 0.744294 days. We create a synthetic model of system using PHOEBE from which we find a mass ratio of $q = 0.55 \pm 0.01$, an orbital inclination of $\theta = 76.19^0 \pm 0.01^0$ and effective temperatures of $T_1 = 6300 \pm 582$ K and $T_2 = 3800 \pm 152$ K for the primary and secondary stars, respectively. In addition we find evidence for an accretion disk caused by streaming of matter from the secondary to the primary.

Key Words

instruments: remote telescope — planetary systems: transits — stars: binaries — stars: Algol systems — mechanisms: mass transfer.

Acknowledgments

Contents

List of Figures

List of Tables

Introduction and Background on Algol Binaries

A binary star system consists of two stars orbiting each other through their mutual gravitational interaction. These systems, as seen from earth, are categorized into two groups: eclipsing and non-eclipsing binaries, based on the inclination of their orbital plane. Eclipsing binary systems produce a variable light curve that can be photometrically analyzed to reveal some of the details of the binary system as seen in figures 1 and 2.
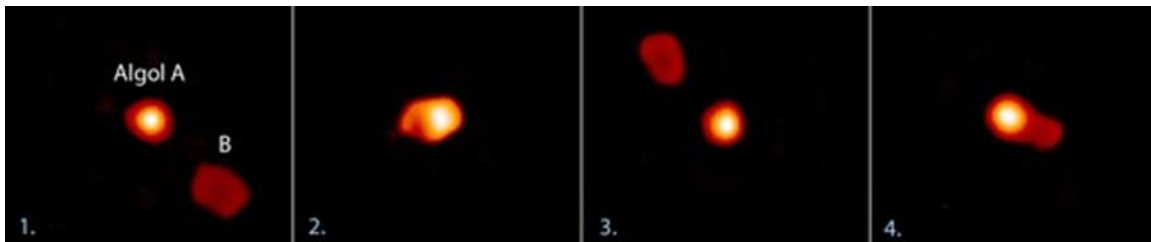
Figure 1: The stars Algol A (center) and Algol B photographed with Georgia State University's Center for High Angular Resolution Astronomy (CHARA) interferometric array on Mount Wilson, California. The larger, cooler B star swings in front of and then behind the smaller, hotter A star.

Eclipsing binaries play major roles in modern astrophysical research. They provide fundamental data on the masses, radii, ages, atmospheres, and interiors of stars as well as serving as astrophysical laboratories for stellar evolution models. The study of eclipsing binaries also provides central information about the formation and evolution of close binaries themselves. Studying the changes in their periods provides insights into evolution of close binaries, mass exchange and loss as well as the discovery of third unseen, low mass bodies. We can trace the beginning of the study of eclipsing binaries (EBs) with the discovery of Algol seen in figure 1, also known as β Persei, to the observations of John Goodricke in 1783. Without eclipses important physical characteristics of the component stars, such as mass, radius, temperature, and luminosity, could not be determined (Andersen 1991, Guinan and Engle 2012). Observations of Algol, however, presented a paradox to astrophysics in that it did not appear to follow accepted models of stellar evolution.
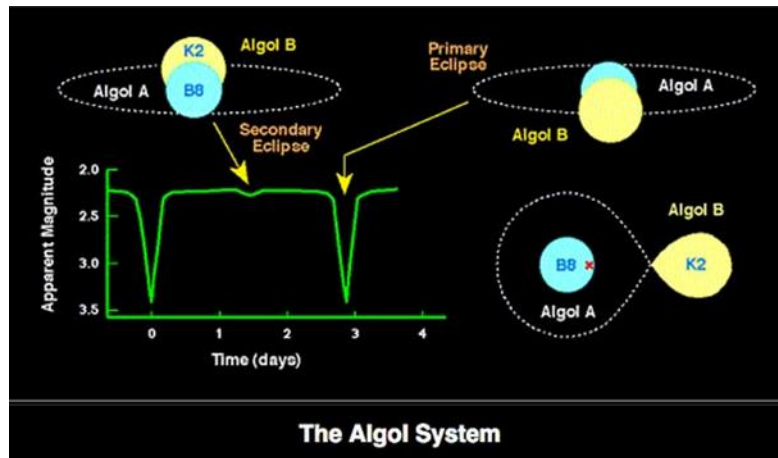
Figure 2: Here's what an eclipse would look like if you could see it up close. The primary eclipse (at right) occurs when the larger but dimmer companion star, a K2 orange subgiant, partially eclipses Algol A, a more massive but smaller main sequence star. A ssecondary eclipse occurs when the cooler star is partially obscured by the hotter star. l

Typically, the more massive a star, the faster it will consume its supply of hydrogen in its core, and, consequently, the faster it evolves. When a star exhausts its core hydrogen, it moves into the red giant stage as hydrogen shell fusion and, later, helium fusion, sustain the star. In the formation of a binary, the stars form, that is, reach the Main Sequence at approximately the same time (within thousands of years). Consequently, the more massive star in a binary system is expected to be more evolved. In the case of Algol, however, the lower mass star was observed to be a red giant and the larger mass star was still an unevolved star on the main sequence.
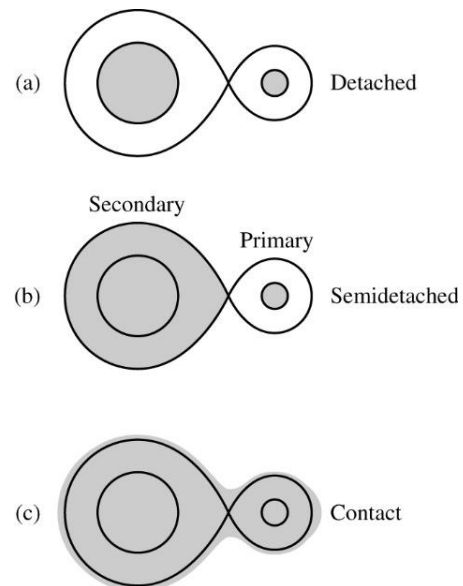
Figure 3: The basic types of binaries classified by how the stars fill their respective Roche lobes. Binaries are classified as detached, semi-detached, and contact based on the sizes of the stars and how they fill their Roche lobes (Ref.: Introduction to Modern Astrophysics, 2nd ed.,Carroll and Ostlie).
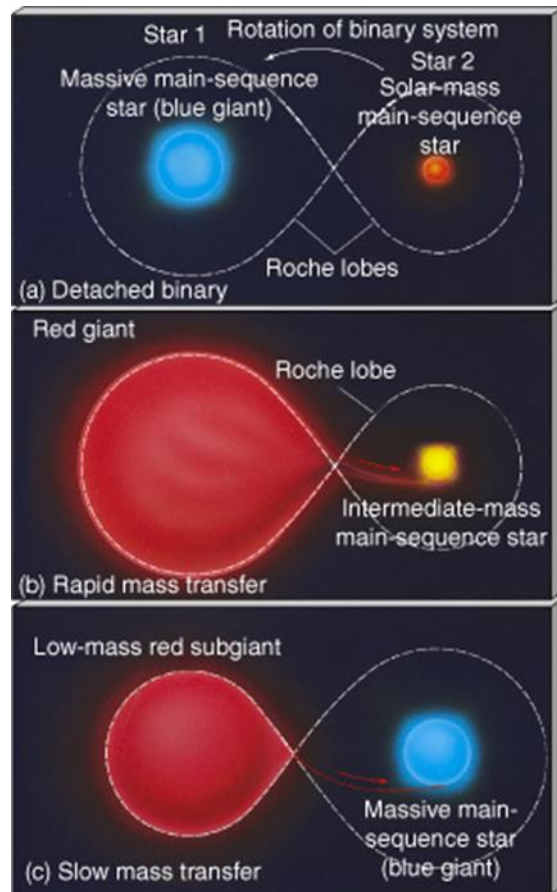
Figure 4: The Massive star consumes the Hydrogen at its core and expands into a red giant. While expanding it exceeds the limits of its Roche Lobe and mass rapidly begins flowing into its neighboring star. After many years of this flow the transfer has slowed significantly and the red giant's Roche lobe has decreased in size as its mass has been drained. (Ref: http://astronomy.nju.edu.cn/~lixd/GA/AT4/AT420/HTML/AT42006.htm)

The problem with the Algol system was resolved when astrophysicists realized that mass could be transferred from one star to the other star. This mass transfer is possible when the radius of one component exceeds the limits of its "sphere of influence", known as the Roche lobe (see Fig. 4). This leads to three different types of binary system; systems in which both stars are completely within their respective Roche lobes are known as detached binaries (see Figs. 3a and 4a). Systems in which one or both of the stars exceed their Roche lobes are known respectively as semidetached and contact binaries (see Figs. 3b, 3c, 4b and 4c). The Roche lobes define the upper limit for the volume of each star for which all its matter is under its own gravitational

influence. The gravitational potential (ϕ) at any point near the binary system can be calculated from the masses of the two stars and their distance from each other and the point in question. ϕ can be calculated using Eq. (1):

$$\phi = -G\left(\frac{M_1}{S_1} + \frac{M_2}{S_2}\right) - \frac{1}{2}\omega^2 r^2 \tag{1}$$

Where G is the gravitational constant, M_1 and M_2 are the two star masses, S_1 and S_2 are the distances from the point to the center of each star's mass, ω is the angular frequency of the binary system, and r is the distance from the measurement point to the system's center of mass. Using this equation, we can find certain points where the gravitational potential is lowest or highest. These points are called Lagrange points. A mass placed at a high Lagrange point tends to fall away from that point into the surrounding area, like a ball on a hill. However, these Lagrange points dictate points where the gravity from each star is cancelling itself out. So, like a ball balanced on a hill without falling in any direction, mass can stay relatively stable if it is at the exact position of a Lagrange point. The location of the most important Lagrange point L_1 is found just between the two stars, a distance l_1 from M_1 and l_2 from M_2. These distances can be found using Eqs. (2) and (3):

$$l_1 = a[0.500 - 0.227\log_{10}(\frac{M_2}{M_1}) \tag{2}$$

$$l_2 = a[0.500 - 0.227\log_{10}(\frac{M_2}{M_1}) \tag{3}$$

At the L_1 Lagrange point, the gravitational and centrifugal influences of both stars cancel each other and allow matter to flow from one star to the other through this point. In a binary system the Roche limits are stretched towards a star's companion due to the gravitational attraction of the sister star. The two Roche lobes of a binary system join at the L_1 Lagrange point of the system. If either star's radius exceeds its stretched Roche limit, mass will escape that star and pass through the Lagrange point and into the Roche lobe of the companion star. This process is

called mass transfer (see Fig. 5). As a result, the more massive star evolves faster and expands but loses its mass to the less massive star, until the less massive star becomes more massive and begins evolving faster than the initially more massive star (see Table 1).
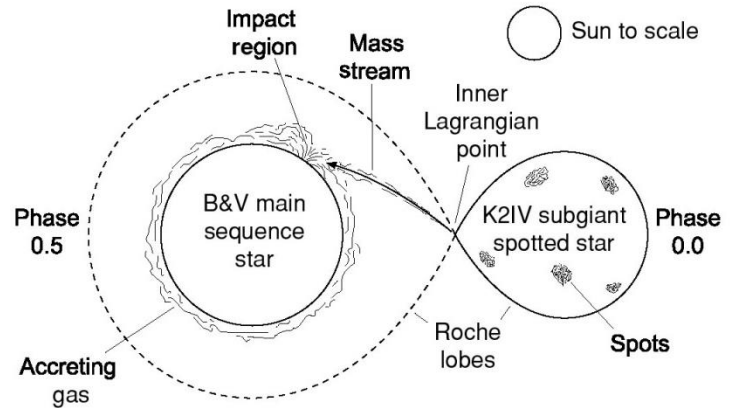
Figure 5: Diagram of mass transfer between a K2IV Subgiant and a B&V Main Sequence Star, the subgiant's radius had exceeded its Roche lobe and is therefore losing mass to the B&V main sequence star. This is a semi-detached binary

BINARY EVOLUTION SEQUENCE		
PHASE	**What Happens**	**Example**
1	**M_1 and M_2 contract**	BM Ori
2	**Both stars on main sequence**	
	- detached	A Cen
	- in contact	W Uma
3	**M_1 evolves and expands**	
	- pre-contact	RS Canum Venaticorum
	- rapid transfer	β Lyrae
	- slow transfer	Algol (β Persei)
4	**M_1 completes evolution**	
	- helium stars	KS Per
	- binary planetary nebula nuclei	UU Sge
	- white dwarf + main sequence	V471 Tauri
5	**M_2 evolves and expands**	
	- pre-contact (M_1 = white dwarf) ⇨ symbiotic star	Mira
	- pre-contact (M_1 = neutron star) ⇨ massive X-ray binary	Cen X-3
	- contact (M_1 = white dwarf) ⇨ cataclysmic variables, CV	Nova Cygni 1975
	- contact (M_1 = neutron star) ⇨ low mass X-ray binary	HZ Here
6	**M_2 completes evolution**	
	- Type 1 supernova	Tycho SN, Kepler SN
	- white dwarf + white dwarf	AM CVn
	- white dwarf + neutron star	Long-period binary pulsar
	- neutron star + neutron star	Binary pulsar 1913+16

Table 1: chart of the different phases and types of phases throughout the evolution of a binary system. Adapted from Trimble, V. 1983, Nature 303, 137.

Method

Data Acquisition

The Small Telescope Exoplanet Transit Search (STExTS) project at the University of Dallas has been in operation since 2012. For approximately 35 nights each summer, the team observes the same single patch of sky through wide-angle astrographs, in order to gather data on a large number of stars over an extended period. Since 2015 the project has configured the telescopes for remote observing at the University of North Texas Monroe Observatory outside Gainesville, TX and the Dark Sky Observatory

Figure 6: Photo of Castor and Pollux, the two telescopes used at the DSOC. They are mounted on the same mount so only Castor was controlled, Pollux only served to obtain extra data.

Collaborative (DSOC) near Ft. Davis, TX. In 2017, time-resolved CCD photometry was conducted with two remote telescopes: Castor and Pollux. These two telescopes were astrographs with focal lengths of 750 mm and focal ratios of 4.8. They were equipped with SBIG ST-10 CCD cameras and mounted on Paramount MEII mounts. They were set up with DSOC at the Dark Sky Observatory in West Texas. The observatory has various piers for small telescope use as seen in Fig. 6.

Castor was controlled using the software Maxim DL while Pollux was controlled using the software CCD Soft. The mount was controlled using SKY X. The telescope would be slewed to the correct position and then a test image would be taken using Castor; the exact location of

the sky being observed would be found using pinpoint astrometry. After this, the telescope would

be slewed more precisely, and the process would be repeated till the field was satisfactory and

the desired star was centered. An example of the usual field centered on GSC 1627-2891 can be

seen in the color inverted figure 7.
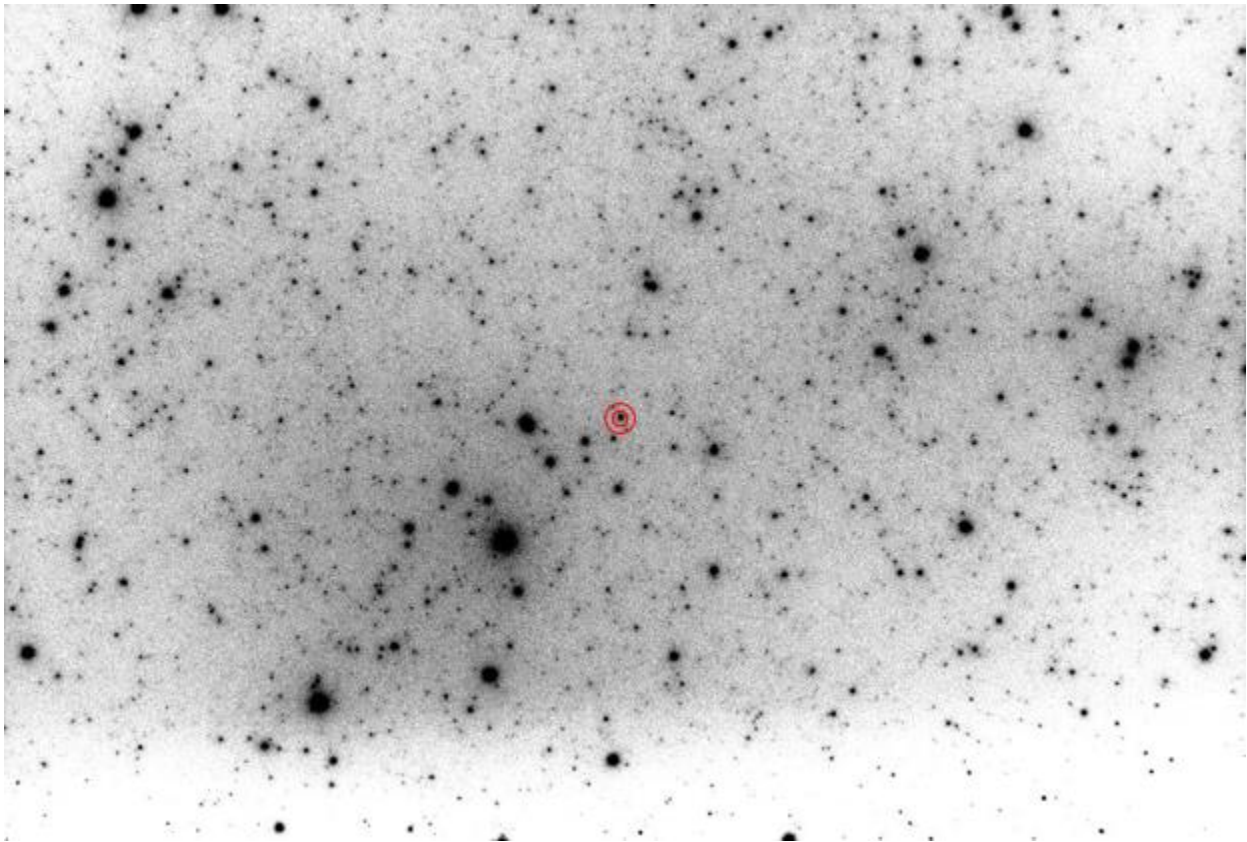
Figure 7: Color inverted field of view for Castor before the nightly meridian flip. Circle superimposed on the image marks the target star GSC 1627-2891. The telescope would be centered on this star for most of the night, allowing any of the nearby stars to be watched and compared to find variable stars.

Once the correct field was obtained a guide star would be calibrated and set tracking.

After this Castor and Pollux would be set taking four minute exposures. Pollux took images of a

portion of the sky seen by Castor after the meridian flip, and after the flip Pollux took images of

Castor's field from before the flip. When observing exoplanetary transits only Castor would be

used to take ninety or eighty-five second exposures to prevent saturation.

The data used to model the Algol system was obtained from *Kepler* Campaign 10. The

Kepler object EPIC KIC 201325107 has been observed once before and was logged as LINEAR 2882780. It is located in the constellation Virgo at Right Ascension 12 h 02 m 05.17 S, and Declination -02° 04' 36.5". The studied light curve begins at BJD 2749.5898 and ends on BJD 2818.7104.

Data Analysis

AstroImageJ Analysis

AstroImageJ is a program that compares the light intensities of stars in astronomical images. A stack of multiple images of the same section of the sky are uploaded along with a set number of black and flat images for the software calibration. AstroImageJ begins by presenting the field of stars captured in the image and allows the user to select and place apertures over the stars with variable light curves that he is observing as seen in Fig. 8.
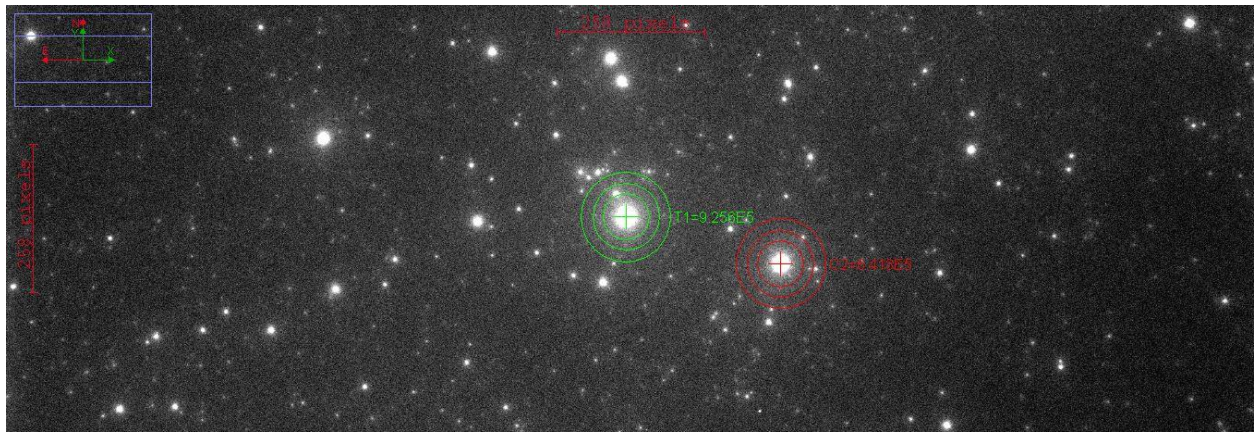
Figure 8: An image of the AstroImageJ interface, showing the star view of HD 189733b for aperture placement. The three apertures selected can be compared after data analysis. Aperture T1 (green) is placed over HD 189733b while C2 (red) is placed over a non-variable nearby star for a light curve comparison.

These apertures track how much light falls within them contrasted with how much light falls in a background area outside of them. The user also selects multiple non-variable stars for flux comparison. The software then applies the same apertures to every image in the stack and produces a data sheet with the light intakes for each of the apertures in each of the images. With

this data, the user can observe the exact variations of the light from a star as the images progress. The software allows the user to compare the intake light of the multiple different apertures chosen and produces beautiful plots of the different apertures as seen in Fig. 9.
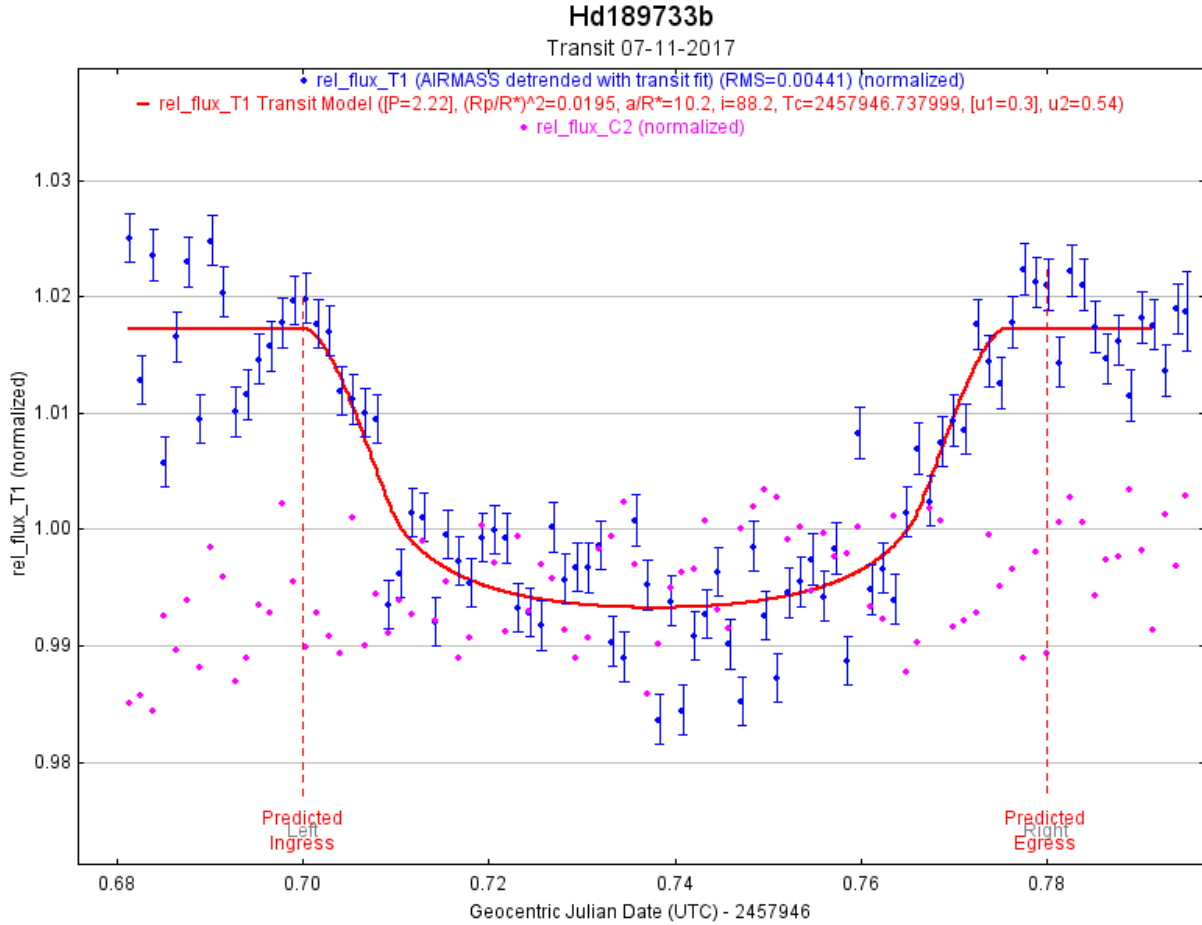
Figure 9: Example plot from data analyzed by AstroImageJ. The plot shown displays the transit of exoplanet HD189733b observed by Castor on 07/11/17

Kepler K2 EPIC KIC 201325107 Analysis

The *Kepler* mission's primary science objective is to discover exoplanets, particularly Earth-sized and in the habitable zone of stars. The spacecraft's Earth-trailing orbit allows it to continuously monitor the field of view and makes it ideal for long term (~72 days) observations of cataclysmic variables (see Fig. 10). The shutter less photometer on the spacecraft has a response function covering the wavelength range 400 – 900 nm and a 116 deg^2 field of view with

a frame time (integration time plus read time) of 6.54 s. In the long cadence (LC) mode, 270 integrations (30 short cadence points) are summed onboard the spacecraft for an effective 1765.5 s or 29.4 minute exposure. Further details can be found in the *Kepler* Data Release Notes 20 (Thompson et al. 2013).
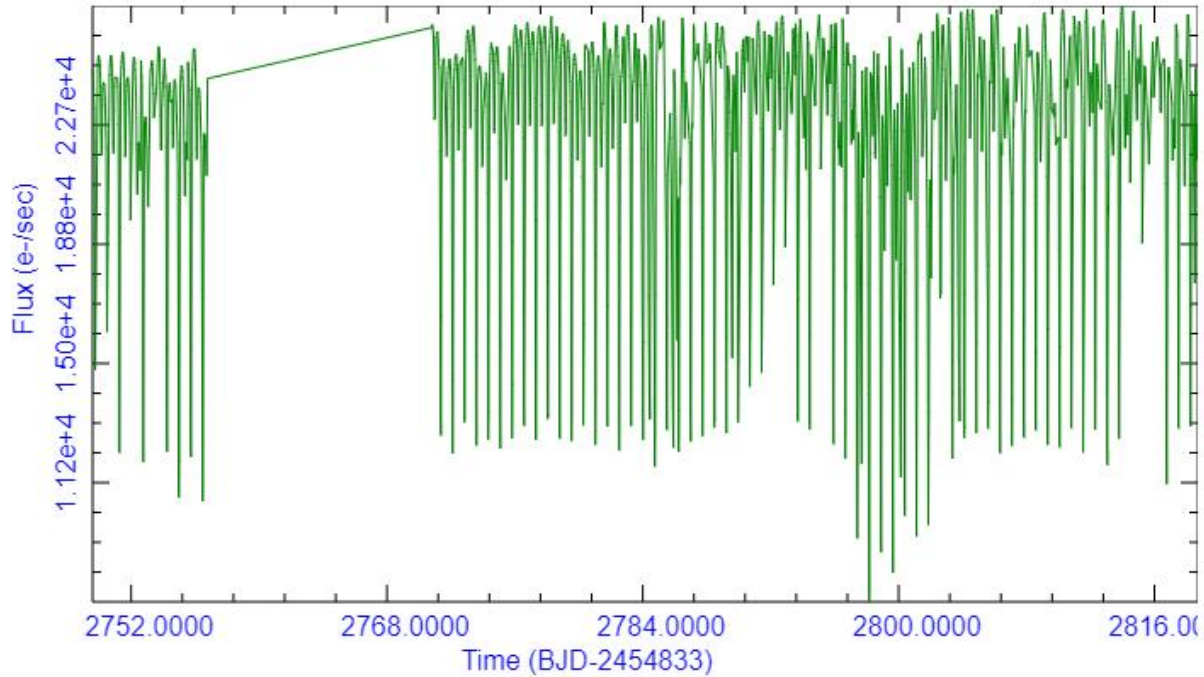
Figure 10: Full KEPLER K2 KIC 201524107 light curve showing the Sap Flux (e-/sec) over 69.12 days taken from the long cadence data from campaign 10.

The precision and accuracy of the time assigned to a cadence are limited by the intrinsic precision and accuracy of the hardware and the promptness and reproducibility of the flight software timestamping process. The flight system requirement, including both hardware and software contributions, is that the absolute time of the start and end of each cadence shall be known to ±50 ms. This requirement was developed so that knowledge of astrophysical event times would be limited by the characteristics of the event, rather than the characteristics of the flight system, even for high SNR events.

The value of BJD (~2.5 million days) is too large to be stored with millisecond precision

in an eight-byte, double precision, floating point number. To compensate, *Kepler* reports the value of BJD-2454833.0. This time system is referred to as Barycentric Kepler Julian Date (BKJD). The offset is equal to the value of JD at midday on 2009-01-01. BKJD has the added advantage that it is only used for corrected dates, so it is more difficult to confuse BKJD dates with uncorrected JD or MJD.

Peranso Analysis

Once obtained, the *Kepler* data had to be analyzed using the software Peranso. The data was copied to an Excel spreadsheet, where all the null and void data points were removed and all extraneous data besides the light flux measurements and the HSC time of each measurement was removed. Peranso was used to graph the remaining *Kepler* light curve. Astronomical data is frequently irregular; in the case of KIC 201325107 the loss of a module caused a large gap in the data. For this reason, a special kind of Fourier transform which copes with gaps in the data is helpful for detecting definite periodical behavior in astronomical light curves (see Fig. 11). The Lomb-Scargle transform, developed by Lomb in 1976 and improved by Scargle in 1982 performs this task (Lomb, 1976 & Scargle, 1982). It turns a light curve into a power spectrum by using the least squares fit value of a sinusoid fitted to the data (Vityazev 1997). The result is a transform that aims at minimizing the difference between observed and modeled data. The
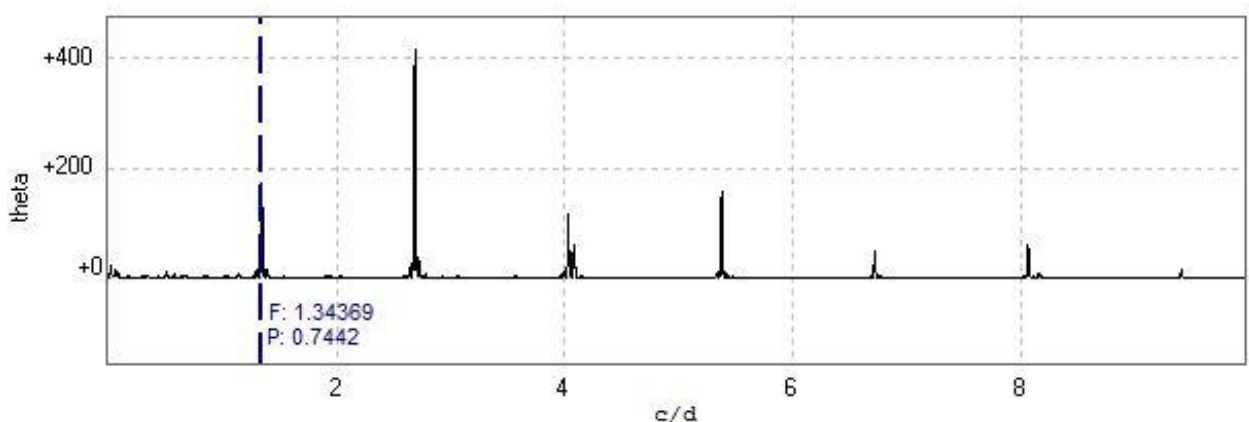
Figure 11: A Fourier transform of the Kepler KIC 201325107 in Peranso produced a Lomb Periodogram which allowed for a close approximation of the period of the system. The blue dotted line indicates the period currently being observed in the Lomb Periodogram phase plot.

Lomb-Scargle transform used by Peranso is optimized using the Horne and Baliunas method (Horne and Baliunas 1986). The Lomb-Scargle method is quite powerful for finding weak periodic signals. This graph displays the power of signals at different frequencies where the power is proportional to the square of the amplitude of the particular signal. This allowed for

close analysis of the most likely orbital period times. The exact orbital period would be marked on this Fourier transform as a severe spike in signal strength in response to the regular amplitude dips in the light curve. The graph produced multiple spikes, one of which was the correct orbital period of the system. The others were harmonics of the orbital period. The largest peak occurred at the point where the primary and secondary light curve minima overlapped, producing double the correct number of amplitude dips at half the orbital period. As Peranso displayed the Fourier transform PDM plot, it simultaneously portrayed a phase plot of the data. The phase plot showed the light curve data folded over upon itself again and again after each orbital period had elapsed. The phase plot orbital period and frequency corresponded to a vertical dotted blue line set on the PDM periodogram (seen on Fig. 11). This could be moved slowly along the periodogram until the phase plot showed all of the amplitude dips aligned. The double period showed a plot with a large dip and a small dip occurring at the same time, making it clear that it was not the correct orbital period. ($P = 0.7442$ days) the phase plot displayed two clear dips, one primary and one secondary, as seen in Fig. 12.
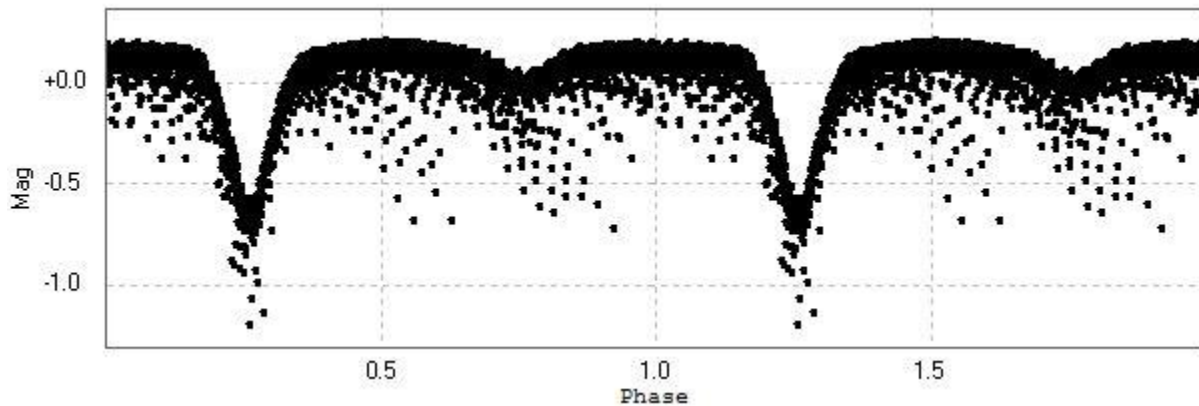
Figure 12: Peranso displayed a phase diagram next to the Lomb periodogram which allowed the user to observe a phase plot of the data at each of the period's he highlighted in the Lomb periodogram. The plot here shows all of the primary minima aligned (where the collective data dips severely) and all the secondary minima aligned (at the smaller dip). The phase plot shown here is the KIC 201524107 data at P=0.7442

13

O – C Analysis
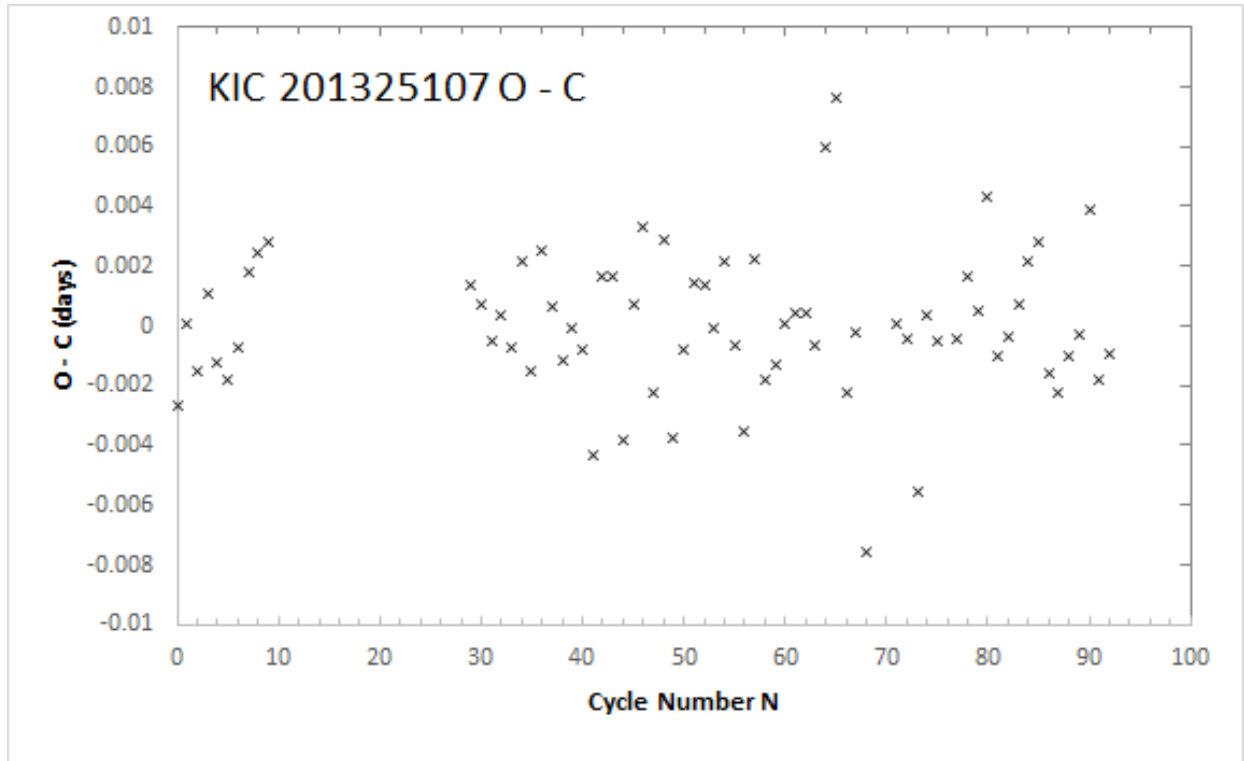
Figure 13: Graph of the residuals from the observed (O) minus calculated (C) minima over the cycle number. This method allowed the orbital period to be determined much more precisely to P = 0.744294 days

After determining the correct orbital period, an O-C process was used to hone it to a more precise value. Each individual maxima and minima of this light curve were painstakingly selected, and an algorithm was used to model a fifth-degree polynomial to the curve at the selected maxima or minima. The exact times of each maxima and minima were then copied to an Excel spreadsheet and saved as the observed values of the periods. The primary minima were considered to be the period of the systems rotation. The secondary minima were considered to occur at half-periods. The first observed period was taken as the epoch and set to be the first calculated period. The period value in Peranso was then added to the first calculated period value to create a list of calculated period times (C). These calculated periods were then subtracted from the observed periods (O) to make an O-C curve opposite the number of periods (see Fig. 13).

An O-C curve allows one to see if the period of the system is increasing or decreasing over time. The period would change gradually if mass-transfer was taking place. The epoch and period were calculated to a greater precision by setting a linear fit to the O-C curve and making slight changes to the period and epoch until the linear fit was zero along the O-C axis, meaning the absolute values of the O-C residuals were at a minimum as seen in Table 2.

Cycle Number (N)	Observed Time	Error in Time	Intensity at Minima	Calculated Time	O-C
0	2749.775	0.01281	-0.524023	2749.777502	-0.002796
1	2750.522	0.00649	-0.704577	2750.521792	-7.12E-05
2	2751.264	0.00527	-0.626719	2751.266082	-0.0016574
3	2752.011	0.00544	-0.714165	2752.010373	0.0009294
4	2752.753	0.00479	-0.660287	2752.754663	-0.0013388
5	2753.497	0.00559	-0.649862	2753.498953	-0.001904
6	2754.242	0.00448	-0.646779	2754.243243	-0.0008542
7	2754.989	0.00015	-0.818035	2754.987533	0.0017046
8	2755.734	0.0048	-0.664295	2755.731824	0.0023584
9	2756.479	0.00348	-0.796914	2756.476114	0.0026872
29	2771.363	0.00533	-0.593085	2771.361918	0.0013482
30	2772.107	0.005	-0.627898	2772.106208	0.00068
31	2772.85	0.0034	-0.606655	2772.850498	-0.0005182
32	2773.595	0.00485	-0.60545	2773.594788	0.0003106
33	2774.338	0.00541	-0.596926	2774.339079	-0.0007596
34	2775.086	0.00552	-0.611103	2775.083369	0.0021872
35	2775.826	0.00544	-0.578081	2775.827659	-0.001542
36	2776.574	0.00289	-0.603032	2776.571949	0.0025108
37	2777.317	0.0049	-0.586063	2777.316239	0.0006646
38	2778.059	0.00279	-0.60275	2778.06053	-0.0011546
39	2778.805	0.00482	-0.585517	2778.80482	-8.78E-05
40	2779.548	0.00546	-0.59776	2779.54911	-0.000772
41	2780.289	0.00303	-0.63947	2780.2934	-0.0042832
42	2781.039	0.00472	-0.611601	2781.03769	0.0017036
43	2781.784	0.0053	-0.563362	2781.781981	0.0016604
44	2782.522	0.00014	-0.651366	2782.526271	-0.0037778
45	2783.271	0.00533	-0.583728	2783.270561	0.000791
46	2784.018	0.00588	-0.574063	2784.014851	0.0033768
47	2784.757	0.00488	-0.66813	2784.759141	-0.0022194
48	2785.506	0.00583	-0.551937	2785.503432	0.0029134
50	2786.991	0.00608	-0.583746	2786.992012	-0.000732

Table 2: Sample of the O-C calculations. The initial time or epoch and the orbital period were altered until the O-C values were as minute as possible.

Modeling with Phoebe

PHOEBE: PHysics Of Eclipsing BinariEs, provides tools to fit a synthetic model of an eclipsing binary system to existing data from such a system. The light curve used in Peranso analysis was copied to a Notepad file, Phoebe was then used to upload the data from the Notepad file and create a light curve shown in Fig. 14.
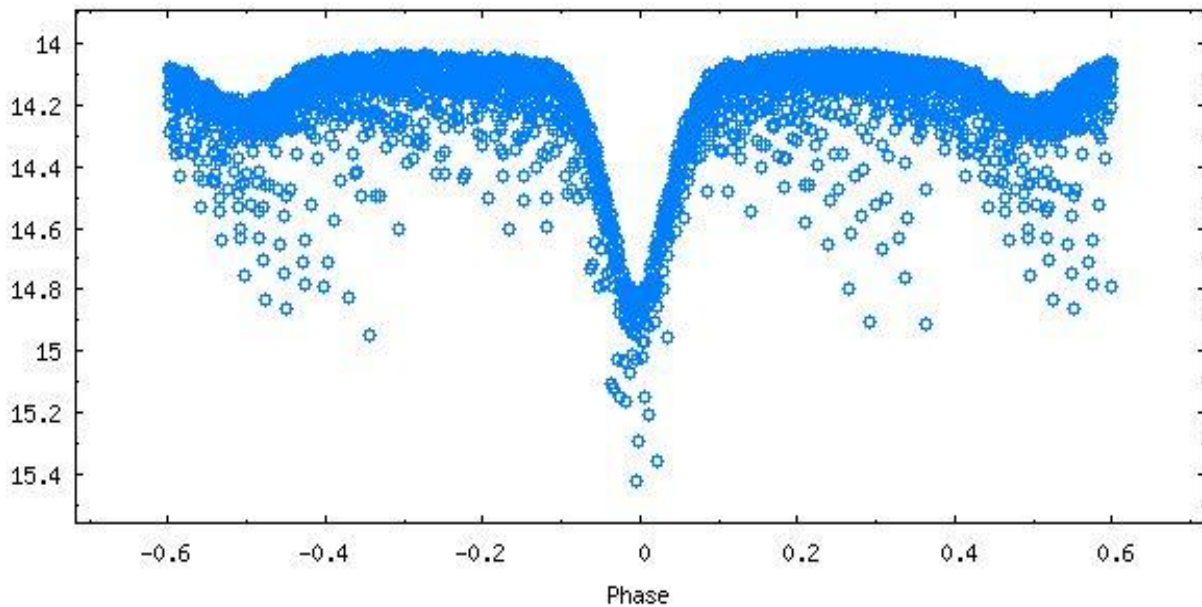
Figure 14: The unaltered KIC 201325107 light curve displayed in the Phoebe- LC plot window. Phoebe LC Plot (light curve plot) does not feature a y-axis label. The y-axis depicts the apparent magnitude.

A synthetic fit curve was then modeled by setting multiple parameters provided by PHOEBE, the primary parameters were the temperatures of the stars, their primary surface potentials, the mass ratio, and luminosities of the stars, and the inclination, and semi-major axis of the system. As the parameters were altered the synthetic light curve approached a close match to the data (see Fig. 15). Eventually the synthetic curve shown in Fig. 16 was produced.
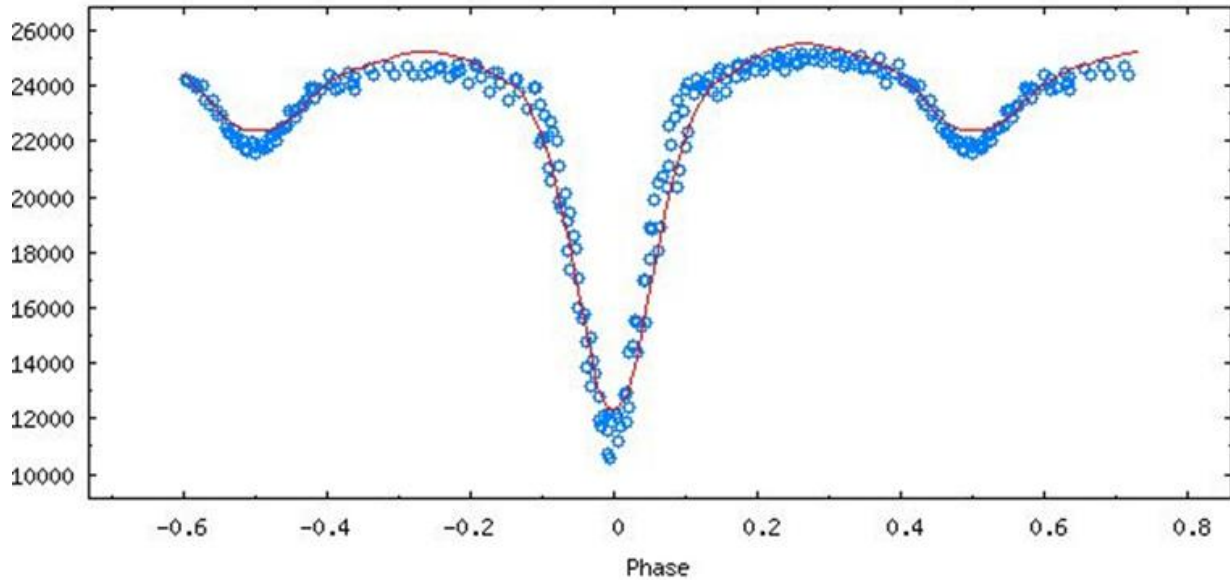
Figure 15: An inferior fit curve, from before the flux data was changed to magnitude data. The synthetic fit needs a few corrections to match the data. A selection of points was used as the synthetic curve was matched to the data.
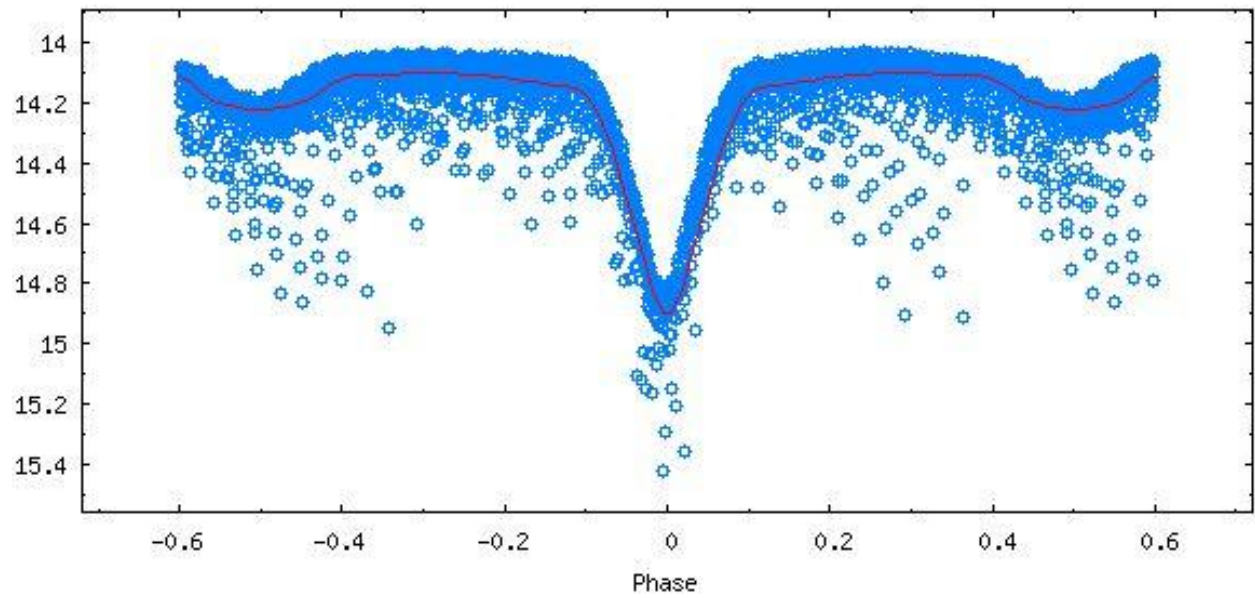
Figure 16: An accurate fit curve shown with the entire data set. The y-axis, though unlabeled by PHOEBE, plots the apparent magnitude of the star. The blue dots are data points and the red line is the synthetic fit curve as modeled by the parameters set in the PHOEBE software.

PHOEBE makes use of the Wilson-Devinney code to help match the synthetic curve to the data points. This code develops a synthetic curve from changeable parameters and then it

uses differential correction to refine those parameters till the synthetic curve is the closest fit to the data. The cost function value, or χ^2 value, reveals how close the fit of the synthetic curve is to the data points. The lower the χ^2 value the closer the fit curve is to the data points (Schniederjan 2013).

The mass ratio of the stars was one of the most important values required for future work. To find a more precise q value, a graph was made by gradually changing the mass ratio and calculating the χ^2 value after every change. The Wilson-Devinney code required some other parameter to be a variable that it could change to achieve its closest value, so the parameter for the argument of periastron was set as the variable that the Wilson-Devinney code could work on, and the mass ratio was the manual variable. The result was a parabolic graph shown in Fig. 17. This shows the mass ratio (q) of the two stars coming down to just around $q = 0.55$. After more precise tests around $q = 0.55$, the smallest χ^2 value was found to be 0.000070 with a few different slightly varying q values, the most likely at $q = 0.5489$.
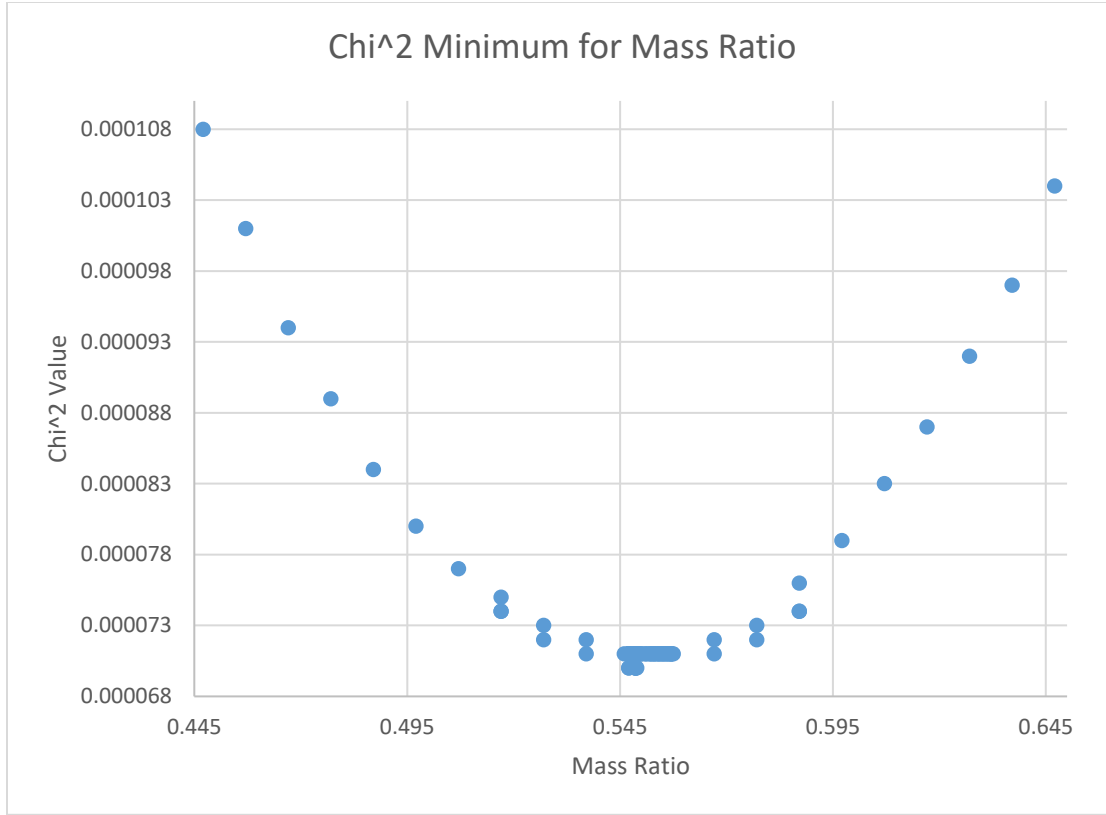
Figure 17: The χ^2 values were plotted for various mass ratios, with multiple mass ratio values being tested at the base of the curve to find the minimum value: q = 0.5489

Discussion

A misinterpretation of the Kepler KIC 201325107 light curve caused a serious setback in the processing of the data. The PHOEBE application had no specific flux unit and had no label for the flux axis in its light curve plot. This can be seen in Fig. 18.
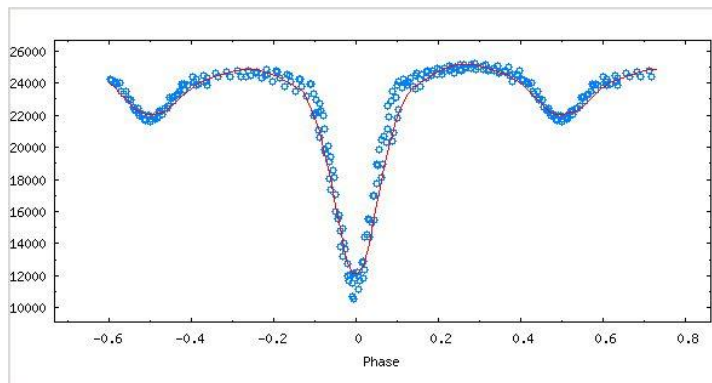
Figure 18: The light curve provided by Kepler had units of e-/sec, while the PHOEBE flux was calculated in units of standard flux.
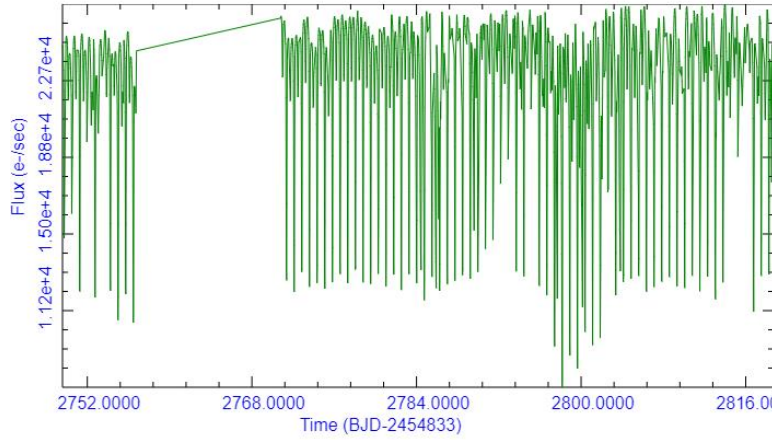
Figure 19: The Kepler data was provided with units of intensity (e-/sec), which were not recognized by PHOEBE software.

The *Kepler* light curve shown in Fig. 19 displays the flux in units of electrons per second (e⁻/sec). As a result, PHOEBE read the Kepler data which ranged from 30000 *e⁻/sec* to less than 5000 *e⁻/sec* as an extremely bright primary star paired with a comparably dim counterpart. As PHOEBE tried to cope with this inconsistency between its flux and the Kepler flux, very strange things began happening to the model, the secondary star took the primary stars place, becoming hotter, larger, and more massive, but the luminosities became 6183.091 $L_\odot$ for the primary star and 99.941 $L_\odot$ for the secondary star. With these luminosities the χ^2 cost function from the Wilson-Devinney code was 124666252.652 from 226 points. To fix this the data set being worked with was converted from flux into apparent magnitude. Kepler's flux converted into an apparent magnitude with the equation:

$$12\ M\ (MAGNITUDE) = 1.72 * 10^5 e^-/sec \tag{4}$$

Every data point we had was converted into apparent magnitude by running it through equation 5:

$$MAGNITUDE = 12 - 2.5 * LOG_{10}\left(\frac{FLUX\left(\frac{e^-}{sec}\right)}{1.72*10^5 \left(\frac{e^-}{sec}\right)}\right) \tag{5}$$

21

Here *FLUX* represents each individual data value from the Kepler data set. This equation converted our data into a PHOEBE-friendly list of magnitude data points that we were able to model with χ^2 fit values between .000075 and .000070. The final model in PHOEBE was produced with the parameters shown in Table 3. The best fit mass ratio was $q = 0.55 \pm .01$. The errors produced in the PHOEBE Nelder & Mead's Simplex fitting method used to get the parameters were greatly underestimated, so to get accurate errors the method was switched to the Differential Corrections method in PHOEBE. Each parameter was run through the Differential Corrections method independently and the errors from this method are shown in Table 3. PHOEBE only provides formal errors for certain parameters (*a*, *P*, *q*, *T(1)* and *T(2)*), but using Eqs. 6 and 7 the errors for each mass were calculated.

$$\sigma_{M1} = M_1 \sqrt{(\frac{3\sigma_a}{a})^2 + (\frac{2\sigma_P}{P})^2 + (\frac{\sigma_q}{q+1})^2} \tag{6}$$

$$\sigma_{M2} = M_2 \sqrt{(\frac{3\sigma_a}{a})^2 + (\frac{2\sigma_P}{P})^2 + (\frac{\sigma_q}{q(q+1)})^2} \tag{7}$$

Parameter	Value	Error	Abbreviation:
Mass Ratio	0.55	$\pm$ 0.01	q
Primary Effective Temperature (K)	6300	$\pm$ 582	Teff (1)
Secondary Effective Temperature (K)	3800	$\pm$ 152	Teff (2)
Inclination (degrees)	76.19	$\pm$ 0.01	INCL
Semi-Major Axis (R$_\odot$)	5.00	$\pm$ 0.09	SMA
Primary Mass (M$_\odot$)	2.0	$\pm$ 0.1	
Secondary Mass (M$_\odot$)	1.09	$\pm$ 0.09	
Primary Radius (R$_\odot$)	1.670691		
Secondary Radius (R$_\odot$)	1.643034		
First Lagrange Point (AU)	2.968696		$\Omega(L_1)$
Second Lagrange Point (AU)	2.644172		$\Omega(L_2)$
Primary Luminosity (normalized)	0.265429		
Secondary Luminosity (normalized)	0.652860		
Primary Surface Potential	3.60477		
Secondary Surface Potential	4.72919		
Primary Surface Brightness	0.071254		
Secondary Surface Brightness	0.004620		
Primary Log(g)	4.574198		
Secondary Log(g)	4.326901		
Eccentricity	0.01001		
Origin of HJD time	2750.525		
Orbital Period (Days)	0.7443	$\pm$ 0.000088	

Table 3: A list of all the values set in PHOEBE to create the synthetic curve seen in figure 16. This curved matched the data curve with the least χ^2 value.

The uncut *Kepler* K2 light curve for KIC 201325107 clearly features an Algol binary, but there are strange points throughout the data set where the intensity of the light curve decreases unexpectedly and then rapidly returns to the usual intensity value. These points decrease in an arc but then reset to the normal intensity immediately as seen in Fig. 20 below the main light curve. A possible explanation is that these anomalies are the result of an accretion disk that is spinning about the primary star. The spin of the disk results in an occasional wobble. This would result in the plane of the disk usually being visible, and occasionally shifting so that only the rim of the disk is visible. When the bright disk is obscured by this shift the light intensity would briefly decrease before the disk straightened and the light intensity returned to its usual value.
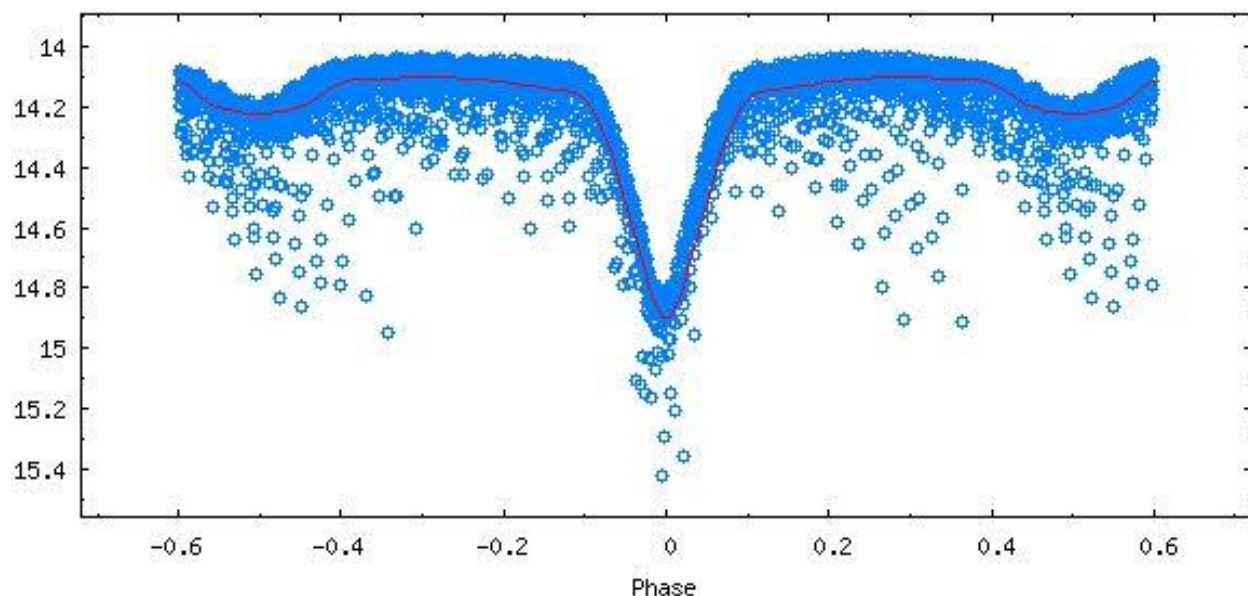
Figure 20: The shape of the Phase Plot of KIC 201325107 shows a clearly defined light curve with strange dips in the data at irregular intervals. These low point anomalies are possibly the result of a rapidly spinning accretion disk.

Loss of Module 4

A complication arises in the C10b data due to the loss of module 4 seven days into C10b (around 2017-07-20 07:00 UT), which powered off the photometer resulting in a 14-day data gap. The cause of the module 4 failure is not known, but the sequence of telemetry faults leading up to the failure and the post-recovery behavior of the focal plane are similar to those seen around the failures of module 7 (January 2014) and module 3 (January 2010). These failures were attributed to a blown fuse in the focal plane local detector electronics (LDE) driver boards, likely due to the failure of an upstream component creating a current over-load.

The C10b spacecraft pointing on either side of this data gap was consistent and at the correct C10 attitude, so flux values should be consistent across the gap. Note that PDC corrected fluxes may show inconsistent systematic error corrections across the 14-day gap, as the co-trending basis vectors can be dominated by systematics present on one side of the gap but not the other side.

The cadences yield Nyquist frequencies that limit the frequency range in which we can discern a signal for interpretation. In the case of LC, the Nyquist frequency equals 24.47 c/d. Other known artifacts are located at the frequencies 0.33 c/d and 7.5 c/d. Kurtz et al. (2015) report a 4.08 c/d artifact due to thruster firings. Moreover, the barycentric correction applied to the spacecraft time shifts the cadences by a nonlinear offset. The effect of the offset is an uneven times series and a shifting Nyquist frequency (Christiansen 2013).

Results

The observations of the starfield surrounding GSC 1627-2891 will be used after processing to discover any variable stars within their field views. These can then be studied in more depth. The light curves of every star will be compared using AstroImageJ in order to detect any slight repeating dip in a light curve. If this occurs it could mean the existence of an extra solar planet, or exoplanet. These can then be closely observed to confirm this observation. The observation of the exoplanet around HD 2882780b by Castor will have to also be repeated a few times to confirm its data and finalize the discovery of the exoplanet there.

The analysis and modeling of KIC 201325107, because it was based on low error *Kepler* K2 data, was able to establish an accurate model of the star system as seen in Figs. 21-28. The values of the most prominent parameters were found to be mass ratio of $q = 0.55 \pm 0.01$, orbital inclination of $\theta = 76.19^0 \pm 0.01^0$ and effective temperatures of $T_1 = 6300 \pm 582$ K and $T_2 = 3800 \pm 152$ K for the primary and secondary stars, respectively. A notable factor of the modeled stars is that the secondary (less massive star) is tidally distorted (see Figs 21-87). It fills its Roche lobe and is very slowly giving mass to the primary star; this distortion gives it a teardrop shape instead of a spherical shape. Because the star is distorted towards it's neighbor it cannot spin

without its mass moving over the distortion for every rotation. This slows its rotation over time and results in one or both of the stars becoming tidally locked. This means that one rotation of a star takes exactly the same time as one orbital period, so the same sides of the stars are always facing each other. Because of this, the side of the stars facing each other become hotter than the rest of the star. To model this, spots were placed in the PHOEBE model system facing the neighboring star. These spots had higher temperatures than the star and allowed for a better fit to the data. Without any data of the radial velocity of the system, it was difficult to produce an appropriate semi-major axis value. To find an accurate semi-major axis, the parameters established by PHOEBE were compared to a star distribution produced by İbanoğlu, and the semi-major axis was set so that the primary and secondary stars were within a reasonable position on these distribution plots (İbanoğlu 2006). The semi-major axis was found to be 5.00 ± 0.09 solar radii ($R_\odot$).
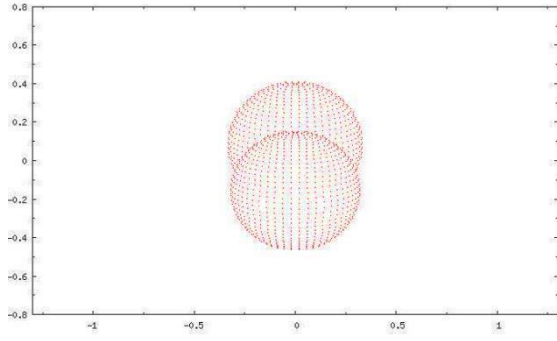
Figure 21: The PHOEBE Modeling Software produces a star shape plot along with the synthetic light curve. Here the stars can be seen plotted in eight different Phases. The Units on the x and y axis are Solar Radii. Phase: 0.0
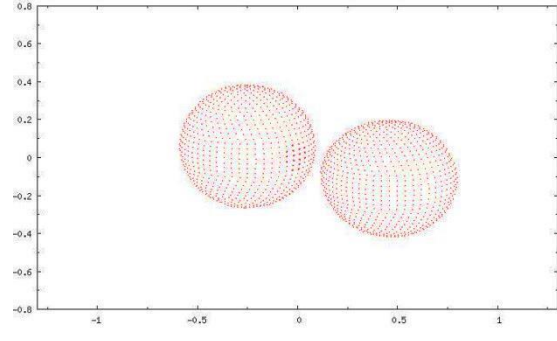

Figure 22: KIC 201325107 Star Shape Plot Phase 0.125, The spots can be seen as very slightly darker areas at the points nearest the adjacent star.
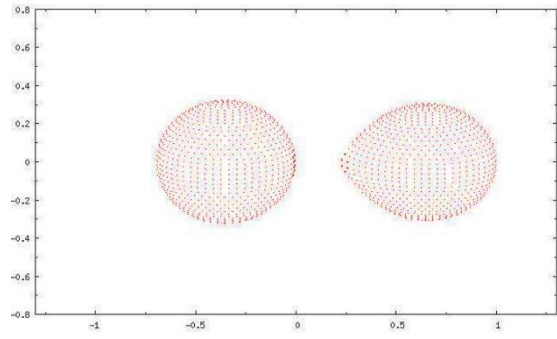

Figure 23: KIC 201325107 Star Shape Plot Phase 0.25
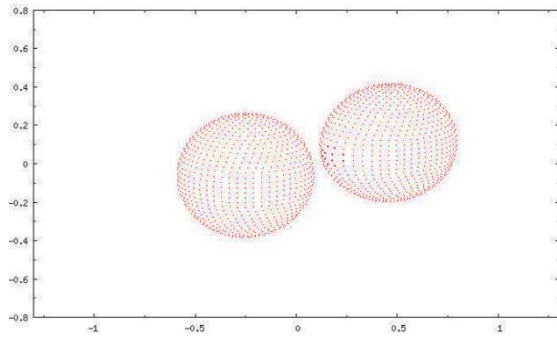

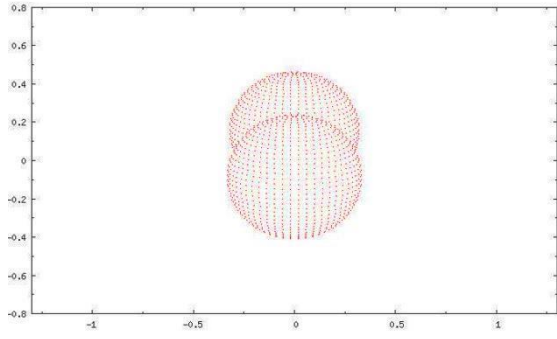*Figure 24: KIC 201325107 Star Shape Plot Phase 0.375*

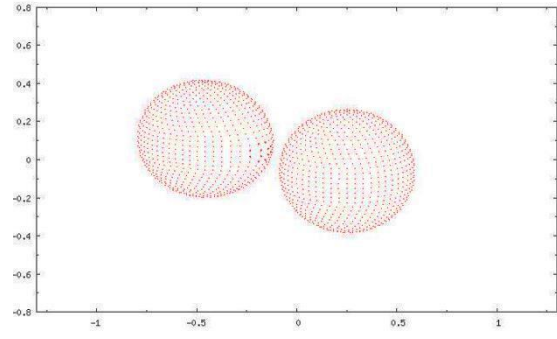*Figure 25: KIC 201325107 Star Shape Plot Phase 0.5*

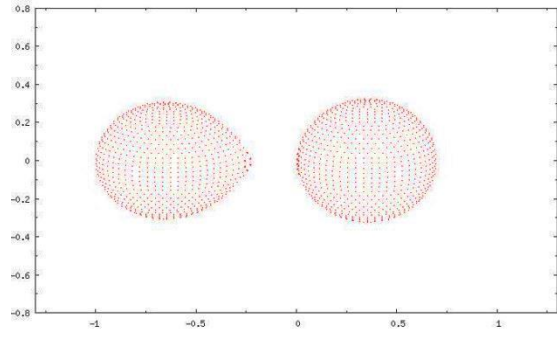*Figure 26: KIC 201325107 Star Shape Plot Phase 0.625*

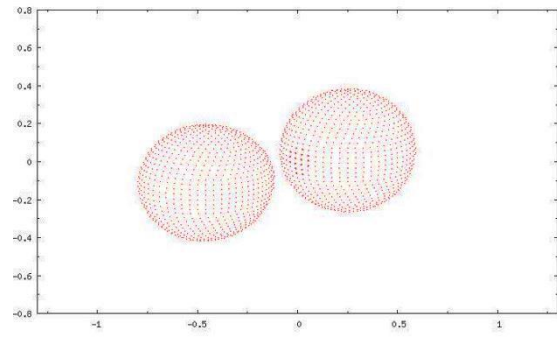*Figure 27: KIC 201325107 Star Shape Plot Phase 0.75*

Figure 28: KIC 201325107 Star Shape Plot Phase 0.825

The mass ratio was tested with extra attention to be sure that it was precise. It can now be used to explore the possibility of an accretion disk surrounding one of the stars in the system. Such a disk is believed to exist and to be spinning rapidly with a wobble. The existence of such a disk explains the anomalies within the full light curve seen in the phase plot in Fig. 29.
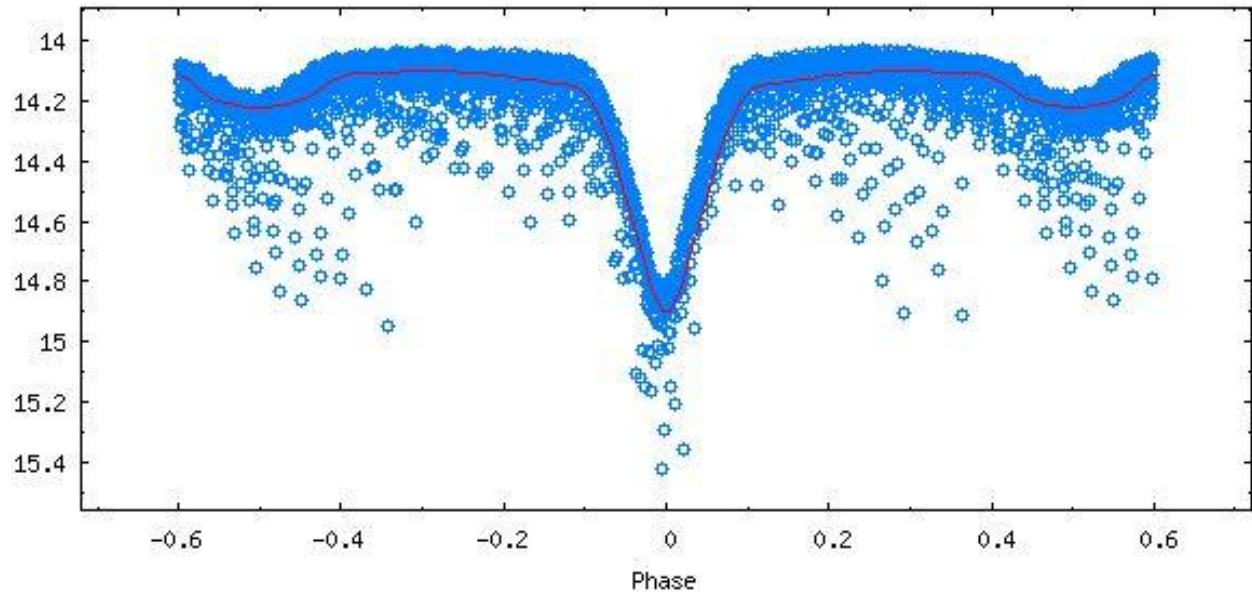
Figure 29: The shape of the phase plot of KIC 201325107 shows a clearly defined light curve with strange dips in the data at irregular intervals. These low point anomalies are possibly the result of a rapidly spinning accretion disk.

The accretion disk would have formed from the matter streaming from one star to the other, the matter would have passed over the first Lagrange point of the system and then would have been caught into the orbit of the receiving star. In this orbit the matter would have formed a bright disk spinning in a plane about the star. The spinning disk would sometimes wobble suddenly so that *Kepler* would see more of its edge and less of its disk plane. This would cause a sudden and temporary decrease in light intensity, leading to the anomalies seen in the light curve data. Fig. 28 displays what might be the standard angle of the accretion disk, a large section of the surface of the disk is visible from earth and the light intensity is consistent. At figure 29, the disk

wobbles so that from earth one can only see the side of the disk and not the surface. This would cause a brief decrease in the stars brightness and would appear as an anomaly in the data set. This is similar to the behavior of accretion disks in star systems where an accretion disk is around a dwarf star. In such cases the disk is much brighter than the star it circles. In the case of KIC 201325107 it is unclear how bright the disk is at present. As a result of this it may be that the disk is cooler and dimmer than the star it circles, in which case the image scene in Fig. 31 would be the usual disk position and the image in Fig. 30 would be the wobbling disk which would eclipse part of the primary star and cause an decrease in light intensity.
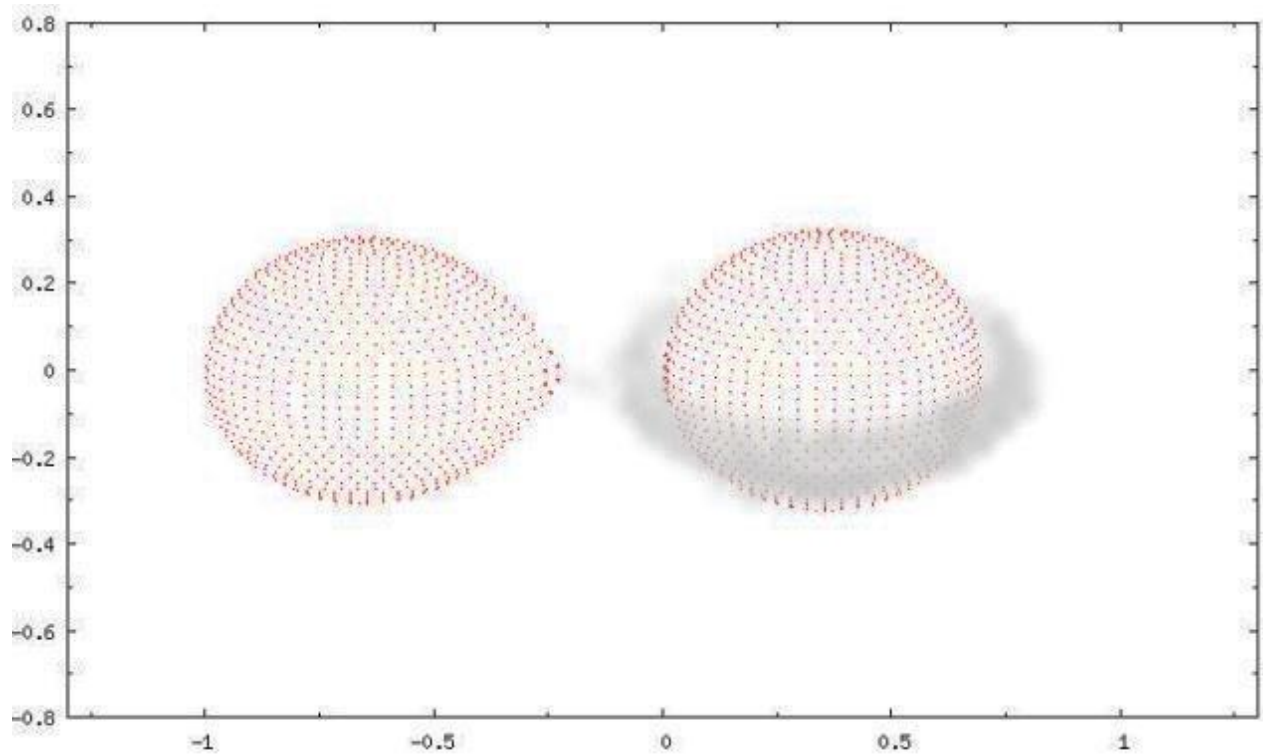

Figure 30: An idea of where the accretion disk might be found around the star. Here the accretion disk is shown in gray and its plane can be clearly seen from the viewers angle.
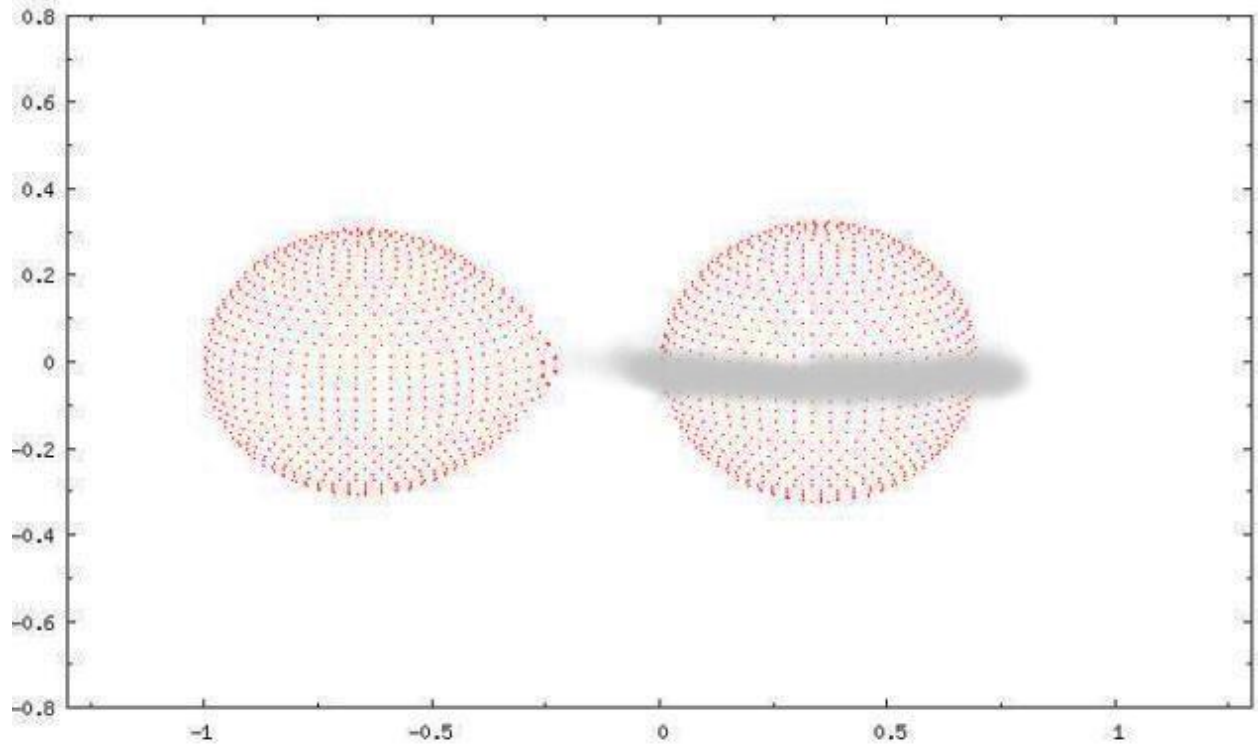
Figure 31: An idea of where the accretion disk might be found around the star. Here the accretion disk is shown in gray and only the disk's rim can be clearly seen from the viewer's angle.

References

Anderson, J., AApR, 3, 91, 1991.

Carroll and Ostlie, *Introduction to Modern Astrophysics, 2nd ed. ,* Cambridge University Press, 2017

Christiansen, J.L. et al., *Kepler Data Characteristic Handbook. KSCI-19040-004.* 2013.

Guinan, E.F., Engle, S.G., Devinney, E.J., JAAVSO, 40, 467, 2012.

Horne, J.H., Baliunas, S.L., ApJ, 302, 757, 1986.

İbanoğlu, C., et. al. MNRAS, 373, 435, 2006

Kurtz, D.W. et al. MNRAS, 450, 3015, 2015.

Lomb, N.R., Ap&SS, 39, 447, 1976.

Scargle, J.D., Ap.J., 263, 835, 1982.

Schniederjan, J. A., University of Dallas, 2013.

Thompson, S.E., et al. *Kepler Data Release Notes. KSCI-19059-001.* 2013.

Trimble, V. Nature, 303, 137, 1983.

Vityazev, V. V., ASP Conference Series Vol. 125, 170, 1997.

Wilson, R.E., ApJ 1, 672, 2008.

Appendices

APPENDIX A: Campaign 10 Proposal to NASA

Summary of K2 Program GO10024

Title: Precession in Algol and Cataclysmic Variable (CV) Close Binary Systems

PI: Montgomery, Michele (University of Central Florida)

CoIs: Goel, Amit; Demasi, Michael; Voloshina, Irina; Richards, Mercedes T, Olenick, Richard

In this proposal, we request of the K2, Cycle 3, Campaigns 8 & 10 to observe two CVs, a CV candidate, and three Algols, all of which have been confirmed to fall on silicon. The goal is to record via the LC mode the long term photometric variability in each of these systems. Long term variability in several CV system types is known to be due to precession -- tidal torques by the secondary star on the disk around the primary star. For the first time ever, Kepler found in previous campaigns a long-term variability in Algol systems, with WX Dra from Kepler Quarters 2-4, 6-8, 10-12, and 14-16 being the poster system. This long term variability has never been observed and confirmed from the ground, necessitating the need for the K2 campaigns. In this work, we hypothesize the source to this long term variability in Algol systems as a precession. Through modeling of the CV and Algol light curves, we aim to determine the type of precession in the Algol systems (i.e., whether prograde or retrograde) and to identify the source to the modulated light (e.g., from a precession of a bright/hot spot hitting a disk around the primary in the Algol, from a precession of a bright/hot spot hitting the primary's photosphere, from a precession of the disk, etc. and not due to star spots or exoplanets). As CVs and Algols share the same dynamics of the mass transfer process in close binary systems and the largest difference between CVs and Algols is the orbital period (or, similarly, the separation distance), this K2 study naturally fits into the long term goals of further establishing the connections between these two types of close binary systems and the evolutions of these star systems. In addition to the K2 observations, we will also observe some of these K2 target candidates (and other like systems) from the ground to establish a photometric modulation baseline. To complete these tasks, we

have put together a team of experts in CVs and Algols and we include two students.

Table 4: Targets requested by this program that have been observed in Kepler K2 campaigns.

EPIC ID	RA (J2000) [deg]	Dec (J2000) [deg]	Magnitude	Investigation IDs
201325107	180.521525	-2.076826	14.046	GO10024_LC
228755638	191.084322	-8.671343	10.763	GO10905_LC GO10004_LC GO10007_LC GO10074_LC GO10024_LC GO10905_SC GO10004_SC GO10007_SC
229021667	188.982657	-1.071315	17.264	GO10024_LC GO10045_LC GO10014_LC GO10024_LC

APPENDIX B: *Kepler* K2 Campaign 10 Details
C10 Pointing
- RA: 186.7794430 degrees
- Dec: -4.0271572 degrees
- Roll: 157.6280500 degrees

The C10a offset from the desired pointing (nominal - measured) was

- delta-RA: 12.12951918 arcsec
- delta-Dec: -4.12973550 arcsec
- delta-Roll: -8.00606815 arcsec

C10a First cadence
- Time: 2016-07-06 19:45:29 UTC
- Long Cadence Number: 128925
- Short Cadence Number: 3856210

C10a Last cadence
- Time: 2016-07-13 01:19:55 UTC
- Long Cadence Number: 129230
- Short Cadence Number: 3865389

C10b First cadence
- Time: 2016-07-13 01:49:21 UTC
- Long Cadence Number: 129231
- Short Cadence Number: 3865390

C10b Last cadence before 14-day gap due to Mod-4 failure
- Time: 2016-07-20 06:26:44 UTC
- Long Cadence Number: 129583
- Short Cadence Number: 3875979

C10b First cadence after gap
- Time: 2016-08-03 06:51:51 UTC
- Long Cadence Number: 130269
- Short Cadence Number: 3896530

C10b Last cadence
- Time: 2016-09-20 04:52:03 UTC
- Long Cadence Number: 132614
- Short Cadence Number: 3966909

C10 Targets
- 41,607 in long cadence (LC)
- 138 in short cadence (SC)
- Custom targets include 16 Solar System moving objects tiled with multiple apertures, 8 bright stars covered with disk apertures to capture the PSF wings, and 27 large galaxies.